RSC Advances

PAPER

View Article Online
View Journal | View Issue

Cite this: *RSC Adv.*, 2015, **5**, 87320

An investigation on the key features of a D–π–A type novel chalcone derivative for opto-electronic applications†

Mohd. Shkir,*[ad] Shabbir Muhammad,*[ad] Salem AlFaify,[ad] Ahmad Irfan,[cd] Parutagouda Shankaragouda Patil,[b] Manju Arora,[e] Hamed Algarni[a] and Zhang Jingping[f]

The current study is focused on the donor–bridge–acceptor (D–π–A) type of novel organic charge transport and non-linear optical material, 1-(4-bromophenyl)-3-(2,4,5-trimethoxyphenyl) prop-2-en-1-one (2,4,5-TMBC) to spotlight its various important properties through experimental and quantum chemical approaches. The compound 2,4,5-TMBC was synthesized *via* a Claisen–Schmidt condensation reaction and its single crystal was grown by a slow evaporation solution growth technique. FT-IR and FT-Raman spectra of 2,4,5-TMBC were obtained and investigated. The molecular geometry of 2,4,5-TMBC was optimized by HF, B3LYP, CAM-B3LYP, wb97xd and LC-BLYP methods using the 6-31G* basis set. The calculated geometrical parameters and vibrational spectra are in good agreement with the experimental results. Time dependent density functional theory (TD-DFT) has been applied to investigate the optical properties of the title compound. The absorption wavelength calculated at the TD-B3LYP/6-31G* level of theory in the gas phase was in good agreement with the experimental value (~400 nm) when compared with other methods. The HOMO–LUMO energy gap was calculated at all the applied levels of theory. The total dipole moment, polarizability, anisotropy of polarizability and static first and total hyperpolarizability values of 2,4,5-TMBC were calculated at different levels of theory. The dipole moment and first hyperpolarizability values are found to be many folds (2 and 56 times calculated at B3LYP) higher than urea. It is also expected that 2,4,5-TMBC would be electron transport material due to its smaller electron reorganization energy value. The study of non-linear optical (NLO) properties shows that 2,4,5-TMBC would be an outstanding candidate for NLO device applications.

Received 9th July 2015
Accepted 25th September 2015

DOI: 10.1039/c5ra13494c

www.rsc.org/advances

1. Introduction

The chalcones (1,3-diaryl-2-propen-1-ones) are open chain flavonoids that are extensively biosynthesized in plants. In recent years, extended scientific research on chalcones fascinating biological properties, such as anti-ulcer, anti-cancer, antimitotic, anti-inflammatory, anti-malarial, anti-fungal, anti-HIV and antioxidant activities, have been carried out.[1–8] Moreover, chalcone molecules have a π-conjugated system that provides a large charge transfer axis. The apposite groups of molecules on the two aromatic rings act as donors and acceptors.[9,10] In such molecules the charges can be transferred from the donor to acceptor through the charge transfer axis. The resilient intermolecular interactions in any molecule give an upswing to second harmonic generation (SHG) efficiency.[11,12] Chalcones have exceptional optical properties, including high extinction coefficients for absorption in the ultra-violet (UV) light region, and noteworthy non-linear optical (NLO) responses.[13–15]

Because of the substantial importance of these compounds, the NLO properties of a series of chalcones have been recently examined experimentally and show encouraging outcomes in future applications such as optical limiters and non-linear frequency conversion.[16–21] To develop such systems for future device applications, it is important to understand the fundamental characteristics of the structural and electronic basis of their optical properties.

To explain the structural and electronic properties in an immense class of materials, ranging from atoms and molecules

[a]*Department of Physics, Faculty of Science, King Khalid University, P.O. Box. 9004, Abha 61413, Saudi Arabia. E-mail: shkirphysics@gmail.com; shkirphysics@kku.edu.sa*

[b]*Department of Physics, K. L. E. Institute of Technology, Opposite Airport, Gokul, Hubli 580 030, India*

[c]*Department of Chemistry, Faculty of Science, King Khalid University, Abha 61413, P.O. Box 9004, Saudi Arabia*

[d]*Research Center for Advanced Materials Science (RCAMS), King Khalid University, P.O. Box 9004, Abha 61413, Saudi Arabia*

[e]*CSIR-National Physical Laboratory, Dr K. S. Krishnan Road, New Delhi 110012, India*

[f]*Faculty of Chemistry, Northeast Normal University, Renmin Street 5268, Changchun, 130024, P. R. China*

† Electronic supplementary information (ESI) available. See DOI: 10.1039/c5ra13494c

to crystals and complex prolonged structures, density functional theory (DFT) has been proved to be tremendously effective and computationally modest. Due to such reasons, DFT has been developed as a mutual contrivance in first-principles calculations directed to predict and describe the characteristic properties of molecular and condensed matter schemes. In recognizing the ingredients and providing information on the composition, structure, conformation, functional groups and intra-molecular interactions in new as well as existing complexes, vibrational spectroscopy has become an excellent tool. DFT provides an irreplaceable spectrum for every definite compound. Many studies have been performed by Hartree–Fock (HF) as well as DFT on various organic, semi-organic, inorganic, chalcones and their complexes and correlated with experimental reports.[22–40]

Recently, Patil *et al.*, have synthesized and grown bulk single crystals of a new NLO chalcone derivative, 1-(4-bromophenyl)-3-(2,4,5-trimethoxyphenyl) prop-2-en-1-one (2,4,5-TMBC), which explores its possible application in NLO devices.[41,42] This chalcone derivative possesses the so-called donor–bridge–acceptor (D–π–A) type structure. The 2,4,5-trimethoxy aryl ring acts as a donor at one end and the 1-(4-bromophenyl)ethanone aryl ring bearing C═O and bromo groups acts as an acceptor at the other terminal end of 2,4,5-TMBC (Fig. 1).

As per the current available literature, no theoretical study has been performed on 2,4,5-TMBC to date, which is necessary to have a complete understanding of the compound from various application points of view.

Therefore, in the current investigation, our aim is to highlight the structural, IR and Raman spectroscopic (experimental and theoretical), electronic, charge transport and non-linear optical properties of the D–π–A type molecule, 2,4,5-TMBC. The obtained results have been compared with the experimental data where available.

2. Experimental details

Initially, the synthesis of 2,4,5-TMBC was achieved by the condensation of 2,4,5-trimethoxybenzaldehyde (0.01 mol) with 4-bromoacetophenone (0.01 mol) in 60 mL of ethanol in the presence of a catalytic amount of sodium hydroxide solution (5 mL, 20%). Continuous stirring was carried out for more than 2 h and then the contents of the flask were transferred into 500 mL of ice-cold water and left to stand for 12 h. The synthesized crude solid was filtered, successively washed with a solution of dilute HCl and distilled water, and then recrystallized more than two times from acetone to obtain the pure chalcone. The synthesized 2,4,5-TMBC was further used to grow single crystals using a solution growth technique with slow evaporation at constant temperature. Further details are available in a previous report.[42]

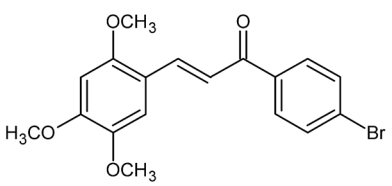

Fig. 1 The chemical structure of 2,4,5-TMBC.

Fourier transform infrared spectra were measured in transmission mode in the range of 4000–400 cm^{-1} using a NICOLET 6700 FT-IR spectrometer at ambient temperature. The samples were taken in KBr pellet form. Each spectrum is an average of 32 scans at 4 cm^{-1} resolution.

Fourier transform Raman spectra of 2,4,5-TMBC were obtained using a Nicolet NXR – FT-RAMAN spectrometer in the 4000–50 cm^{-1} region with a 1064 nm Nd:YVO4 laser as the excitation source.

3. Computational methodology

The optimized and stable geometry of 2,4,5-TMBC has been achieved by DFT using B3LYP (Becke's three parameter exchange functional B3 combined with Lee–Yang–Parr correlation functional LYP)[43,44] and Hartree–Fock (HF) at the 6-31G* basis set. The visualization of the obtained results was performed by the Gauss view 5 visualization program.[45] In addition, optimization of the geometries was also carried out using the CAM-B3LYP, wb97xd and LC-BLYP levels of theory. The stability of the optimized geometry was further confirmed by computing its analytical frequencies. The range-separated functionals were highly dependent on the range-separation parameter. Thus, one way to eliminate these ambiguities was to tune the range-separation parameter (especially for donor–acceptor complexes).[46,47] Moreover, these techniques could make the theoretical calculations match even closer to the experimental results. Furthermore, to calculate the structural parameters in the periodic boundary conditions, we have imported the crystal information file (CIF) and optimized it using a generalized gradient approximation GGA/PBE[48] functional and DNP basis set.[49] DMol3 code,[50] which is implemented in the Accelrys package Materials Studio,[51] has been used to compute the geometries.

The total first hyperpolarizability (β_{tot}) and its components for 2,4,5-TMBC were evaluated using a finite field (FF) approach at all the above mentioned levels of theory. The FF approach has been widely used to calculate the first hyperpolarizability of numerous chemical systems and has provided very consistent results when compared with the experimental data.[52,53] Herein, we have applied various methods, including B3LYP, HF, range separated hybrid functionals, such as CAM-B3LYP and wb97xd, and long range corrected LC-BLYP at the 6-31G* basis set for calculating the dipole moment and first hyperpolarizability, and compared them with each other. In general, in the FF approach, a static electric field (F) is applied and the energy (E) is expressed by the following equation:

$$E = E^{(0)} - \mu_1 F_1 - \frac{1}{2}\alpha_{ij}F_iF_j - \frac{1}{6}\beta_{ijk}F_iF_jF_k - \frac{1}{24}\gamma_{ijkl}F_iF_jF_kF_l - \ldots \quad (1)$$

where $E^{(0)}$ represents the total energy of the molecule in the absence of an electronic field, μ is the vector component of the dipole moment, α is the linear polarizability, β and γ are the second and third-order polarizabilities, respectively, whereas x, y and z label the i, j and k components, respectively. It can be observed from eqn (1) that differentiating E with respect to F obtains the μ, α, β and γ values.

The electronic dipole moment, molecular polarizability, anisotropy of polarizability and molecular static, and first total hyperpolarizability were calculated from the following equations.

For a molecule, its dipole moment (μ) is defined as follows:

$$\mu_{\text{tot}} = (\mu_x{}^2 + \mu_y{}^2 + \mu_z{}^2)^{1/2} \quad (2)$$

Total polarizability was calculated by

$$\alpha_{\text{tot}} = \frac{1}{3}(\alpha_{xx} + \alpha_{yy} + \alpha_{zz}) \quad (3)$$

Anisotropy of polarizability was calculated by

$$\Delta\alpha = \frac{1}{\sqrt{2}}\sqrt{\left[(\alpha_{xx} - \alpha_{yy})^2 + (\alpha_{yy} - \alpha_{zz})^2 + (\alpha_{zz} - \alpha_{xx})^2 + 6\alpha_{xz}{}^2\right]} \quad (4)$$

First hyperpolarizability components of can be evaluated by expression:

$$\beta_i = \beta_{iii} + \sum_{i \neq j}\left[\frac{(\beta_{ijj} + 2\beta_{jii})}{3}\right] \quad (5)$$

Using the x, y, z components, the resultant total first hyperpolarizability (β_{tot}) can be calculated by

$$\beta_{\text{tot}} = \sqrt{\left(\beta_x{}^2 + \beta_y{}^2 + \beta_z{}^2\right)} \quad (6)$$

where β_x, β_y and β_z are

$$\beta_x = (\beta_{xxx} + \beta_{xxy} + \beta_{xyy})$$

$$\beta_y = (\beta_{yyy} + \beta_{xxz} + \beta_{yyz})$$

$$\beta_z = (\beta_{xzz} + \beta_{yzz} + \beta_{zzz})$$

Therefore, the magnitude of total first hyperpolarizability is given by

$$\beta_{\text{tot}} = \sqrt{\left[(\beta_{xxx} + \beta_{xxy} + \beta_{xyy})^2 + (\beta_{yyy} + \beta_{xxz} + \beta_{yyz})^2 + (\beta_{xzz} + \beta_{yzz} + \beta_{zzz})^2\right]} \quad (7)$$

Second-order polarizability (β) is known as a third rank tensor that can be described by a 3 × 3 × 3 matrix. Due to Kleinman symmetry ($\beta_{xyy} = \beta_{yxy} = \beta_{yyx}$, $\beta_{yyz} = \beta_{yzy} = \beta_{zyy}$, … likewise other permutations also take same value), the 27 components of the 3D matrix can be reduced to 10 components.[54] These components have been calculated using GAUSSIAN 09.[55] Similarly, time dependent (TD) with B3LYP, HF, range separated hybrid functional CAM-B3LYP, wb97xd and long range corrected LC-BLYP has been used to estimate the transition energies of the title molecule.

The charge transfer rate can be described by Marcus theory *via* the following equation.[56]

$$W = V^2/h(\pi/\lambda k_{\text{B}}T)^{1/2}\exp(-\lambda/4k_{\text{B}}T) \quad (8)$$

where the transfer integral (V) and reorganization energy (λ) are the main parameters that determine the self-exchange electron-transfer rate and finally the charge mobility. Smaller λ and larger V values would lead to the efficient charge transport properties.

There are two types of λ, *i.e.*, inner λ (molecular geometry relaxation when an electron is added to or removed from a molecule) and outer λ (the variations in the surrounding medium due to polarization effects). Herein, we focused on the inner λ, which shows the geometric relaxation in the molecule. The inner λ can be divided into two parts: $\lambda_{\text{rel}}^{(1)}$ and $\lambda_{\text{rel}}^{(2)}$, which correspond to the geometry relaxation energy of molecule from its neutral to charged state, and from its charged to neutral state, respectively.[57]

$$\lambda = \lambda_{\text{rel}}^{(1)} + \lambda_{\text{rel}}^{(2)} \quad (9)$$

These terms were calculated from the adiabatic potential energy surfaces.[58]

$$\lambda = \lambda_{\text{rel}}^{(1)} + \lambda_{\text{rel}}^{(2)} = [E^{(1)}(L^{\pm}) - E^{(0)}(L^{\pm})] + [E^{(1)}(L) - E^{(0)}(L)] \quad (10)$$

where $E^{(0)}(L)$, $E^{(0)}(L^{\pm})$ are the ground-state energies of the neutral and charged states, $E^{(1)}(L)$ is the energy of the neutral molecule in the optimized charged geometry and $E^{(1)}(L^{\pm})$ is the energy of the charged state in the geometry of the optimized neutral molecule.

4. Results and discussion

4.1. Molecular geometry

The optimized stable molecular geometry of 2,4,5-TMBC by B3LYP using the 6-31G* basis set is shown in Fig. 2(a), further optimization of its geometry was also carried out using the HF, CAM-B3LYP, wb97xd and LC-BLYP levels of theory (see ESI data displayed in Fig. S1(b–e)†). In addition, we have studied the geometrical parameters of 2,4,5-TMBC, applying the periodic boundary conditions in which the calculated geometrical

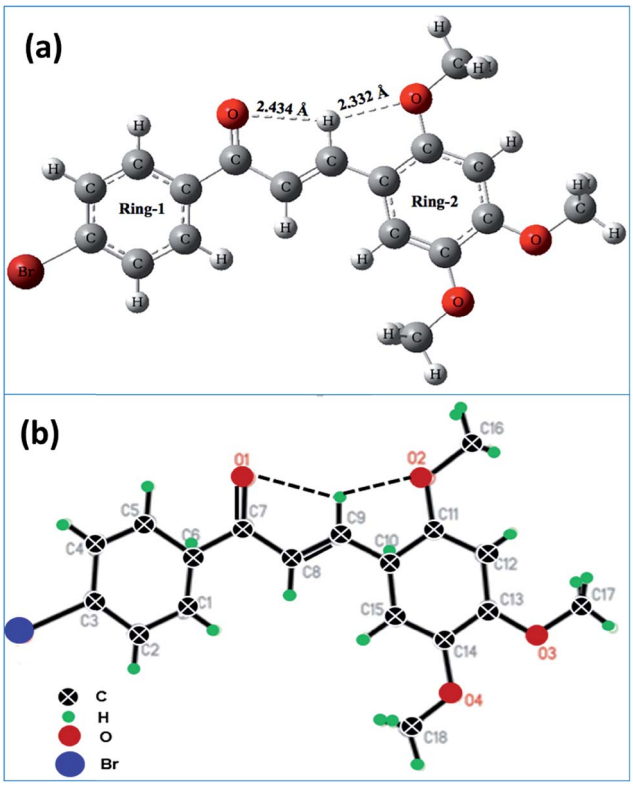

Fig. 2 The optimized molecular geometry of 2,4,5-TMBC. (a) B3LYP using the 6-31G* basis set and (b) the experimentally observed geometry.[41]

parameters were compared with the experimental crystal structure obtained in the solid-state.[59,60] It can be observed that there is intra-molecular bonding between O(3) and H(20) with a bond length of 2.332 Å and between O(2) and H(20) with a bond length of 2.434 Å, obtained by B3LYP, whereas these values calculated by HF were found to be 2.363 Å and 2.448 Å, respectively. These are in close agreement with the experimental values of 2.360 Å and 2.450 Å (presented in Table 1).[41] These geometrical parameters calculated by the periodic boundary conditions at the PBE/DNP level of theory were also found to be in reasonable agreement with the experimental values reported (see Table 1 and Fig. S2†). The three methoxy groups are attached at C(22), C(25) and C(26) in 2,4,5-TMBC, which are almost co-planar with the C(21) and C(27) atoms of the aryl ring. Experimentally, its crystal structure was stabilized by intermolecular C12–H12A···O1^{i} and C16– H16B···O1^{i} interactions (the code of symmetry is given in Table 1) and these interactions generate a ring of graph-set motif R12 (7). The short Br1···O4 $(-3/2 + x, 3/2 - y, 1 - z)$ contact [3.264(2) Å] also favors crystal structure stabilization. The experimentally observed geometry is shown in Fig. 2(b).[41]

All other bond lengths between C–C, C–H, C–Br, and C–O are in good agreement with the available literature.[16,61–64] Table S1 of the ESI† shows the values of the key geometrical factors, including bond lengths, bond angles and dihedral angles, of the optimized 2,4,5-TMBC molecule at the different levels of theory.

4.2. Vibrational analysis

Infrared (IR) and Raman spectroscopy techniques have been extensively used by organic chemists for the identification of functional groups, bonding in different molecular conformations and reaction mechanisms by tentatively assigning their observed fundamental modes.[65–72] In vibrational spectroscopy, the shift in peak position is discussed in terms of the changes in the crystalline field effect induced electronic effects, hydrogen bonding and Fermi resonance electronic effects that arise from back donation and the induction of bonded groups present in a material. Inter-molecular and intra-molecular hydrogen bonding appears when H atoms and N, O or F atoms are present between two molecules or within a molecule. The vibrational modes in the two phenyl rings will differ in wavenumber and the magnitude of splitting will depend on the strength of the interactions between the different parts (internal coordinates) of the two rings. For some modes, this splitting is so small that they may be considered as quasi-degenerate and for the other modes a remarkable splitting is observed.

1-(4-Bromophenyl)-3-(2,4,5-trimethoxyphenyl)prop-2-en-1-one ($C_{18}H_{17}BrO_4$) possesses a orthorhombic structure with $P2_12_12_1$ space group and four molecules per unit cell. The unit cell dimensions are a = 7.3031(3) Å, b = 10.3422(4) Å, c = 21.3355(9) Å, and V = 1611.47(11) Å^3.[41,42]

In the orthorhombic crystal system with the non-centrosymmetric space group $P2_12_12_1$ (D_2^4), the Bravais cell

Table 1 Experimental and theoretical hydrogen-bond geometry (Å, °) parameters of 2,4,5-TMBC

Exp.[41]				Theoretically calculated (present study)									
				B3LYP		HF		LC-BLYP		wb97xd		PBE^b (PBC)	
D–H···A	H···A	D···A	Bond angle	H···A	Bond angle	H···A	Bond angle	H···A	Bond angle	H···A	Bond angle	H···A	Bond angle
C9–H9A···O1	2.45	2.799(5)	102	2.434	98.70	2.448	97.27	2.378	98.73	2.444	97.789	2.461	97.94
C9–H9A···O2	2.36	2.720(5)	103	2.332	100.35	2.363	98.36	2.313	99.68	2.354	98.431	2.315	100.20
C12–H12A···O1^a	2.57	3.470(4)	164										
C16–H16B···O1^a	2.57	3.303(5)	133										

^{a} Symmetry code: (i) $-x + 1, y + 1/2, -z3/2$. ^{b} With periodic boundary conditions (PBC).

Table 2 Factor group analysis of 2,4,5-TMBC

S. No.	Factor group symmetry (D_2^4)	A	B_1	B_2	B_3
1	External modes	6	6	6	6
	(i) Translational modes	3	3	3	3
	(ii) Rotational modes	3	3	3	3
2	Internal modes	114	114	114	114

consists of 4 molecules and occupies the $C_1(4)$ site symmetry. A single molecule of 2,4,5-TMBC contains 40 atoms and 160 atoms in a unit cell. The irreducible representation of the point group where all atoms acquire the C_1 site symmetry is described as follows:

$$\Gamma_{\text{total}} = 120A + 120B_1 + 120B_2 + 120B_3$$

which includes the three acoustic modes corresponding to the block translations of the crystal $\Gamma_{\text{vib, acoustic}} = B_1 + B_2 + B_3$. The formal classification of the fundamental mode predicts that the 456 internal vibrations can be distributed as $(114A + 114B_1 + 114B_2 + 114B_3)$ and the 24 external modes such as $(3A + 3B_1 + 3B_2 + 3B_3)$ translational and $(3A + 3B_1 + 3B_2 + 3B_3)$ rotational vibrational modes. Phonons belonging to B_1, B_2 and B_3 are both Raman and infrared active. The phonons belonging to A symmetry are Raman active and infrared inactive.

The results and summary of the factor group analysis are presented in Tables 2 and 3, respectively.

4.2.1. Internal vibrations. 2,4,5-TMBC does not have any symmetry and so the internal vibrations exhibited are both IR and Raman active exclusive of the acoustic mode. The internal vibrations may be classified as those arising from the CH_2, CH_3, C_6H_5, CH_3O, en-1-one and C–Br functional groups. These vibrations are obtained as a strong bands coupled between themselves.

4.2.2. External vibrations. The external vibrations are generally observed below 500 cm^{-1} due to the rotational and translational modes of vibration of the 2,4,5-TMBC ionic functional groups. The rotational modes are obtained at higher frequency and intensity than the translational modes in the Raman spectra, whereas the translational modes are more intense in the IR spectra.

The theoretical spectra were derived from the B3LYP/6-31G* and HF/6-31G* levels of theory. The experimentally obtained and theoretically calculated spectra of 2,4,5-TMBC are shown in Fig. 3. The theoretically predicted vibrational frequencies have no imaginary frequency, which indicates that the optimized molecular geometry of 2,4,5-TMBC is located at the local minimum point of the potential energy surface. The well-known fact about density functional theory potentials is the overestimation of the vibrational wavenumbers. For a good comparison with the experimental values, scaling was used for the theoretically calculated spectra [for B3LYP it was 0.9613 and for HF it was 0.8929]. The obtained (IR transmittance and Raman) spectra and calculated peak positions of the vibrational modes in wavenumber at both the B3LYP and HF level of theory and their corresponding tentative assignments are listed in Table S2.†

The IR transmittance and Raman experimental as well as theoretical spectra analysis of 2,4,5-TMBC have been made on the basis of the characteristic vibrations of the methoxy group, carbonyl group, methyl group, phenyl ring with *ortho*- and *para*-substitution, bromo-phenyl group and the prop-2-en-1-one bridge. The calculated vibrational wavenumber and the atomic displacement corresponding to the different normal modes were used to identify the ambiguity in the vibrational modes. The computed and experimental IR and Raman wavenumbers corresponding to the different modes are listed in Table S2† along with their detailed assignments. For visual assessment, the experimental and calculated IR transmittance and Raman spectra are presented in Fig. 3. We have tentatively assigned all the vibrational bands. The frequencies of the calculated and observed bands are provided in Table S2.†

4.2.2.1. The methoxy (O–CH_3) group. In the methoxy group, the CH_3 group is directly attached to an oxygen atom, the C–H stretching and bending peak positions can shift either to a higher or lower wavenumber depending on the position and electronic effects of groups to which it is bonded to in the material.[73] In the present case, three methoxy groups are bonded to a phenyl ring at the *ortho*- and *para*-positions. The asymmetric and symmetric methyl stretching bands are observed as very weak intensity components in the 2960–2850 cm^{-1} region at 2952, 2927 and 2852 cm^{-1}, respectively in the experimental IR spectrum and at 2952, 2933 and 2844 cm^{-1} in the experimental Raman spectrum of this sample.[65,66,70] The calculated values of the asymmetric and symmetric stretching modes were found at 2929 and 2855 cm^{-1} (B3LYP), 2867 cm^{-1} (HF) in IR spectra and at 2965, 2910 (B3LYP) and 2925 (HF) cm^{-1} in the Raman spectra. As the calculations were carried out

Table 3 Factor group analysis – summary for 2,4,5-TMBC

Factor group symmetry (D_2^4)	Site symmetry			C18	H17	O4	Br	Optical modes	Acoustic modes
	External		Internal						
A	3T	3R	114	54	51	12	3	120	0
B_1	3T	3R	114	54	51	12	3	120	1
B_2	3T	3R	114	54	51	12	3	120	1
B_3	3T	3R	114	54	51	12	3	120	1
Total				216	204	48	12	480	3

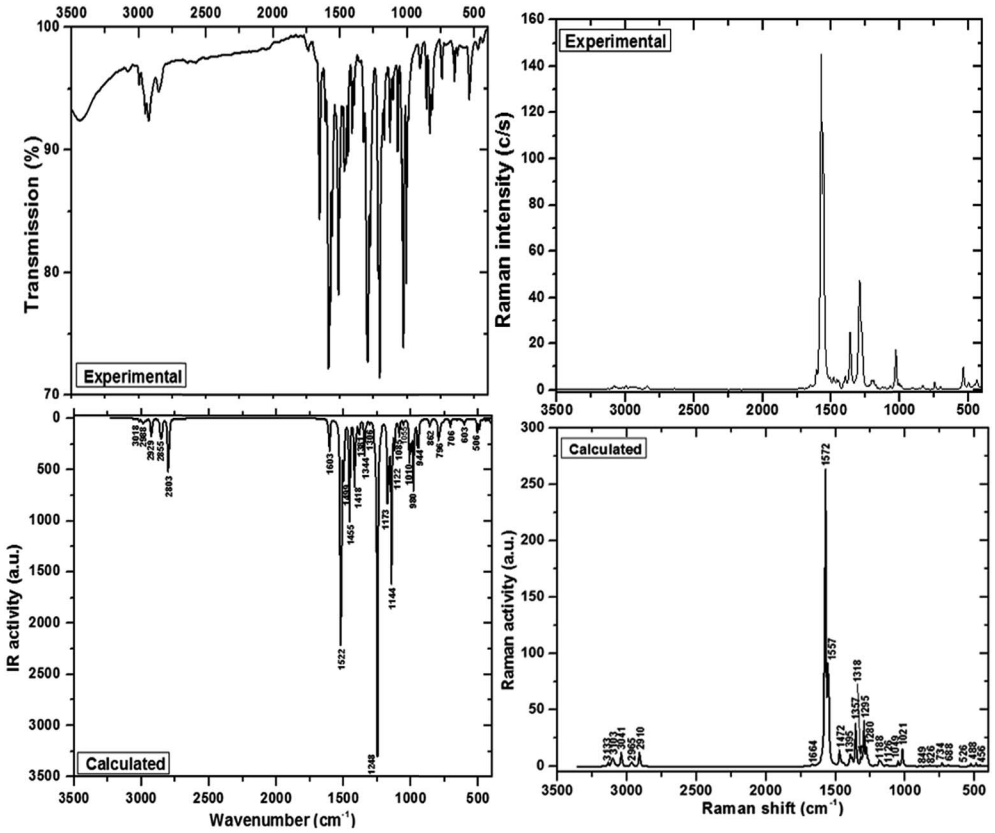

Fig. 3 The calculated and measured (a) IR and (b) Raman spectra of 2,4,5-TMBC.

on a free molecule and the experimental spectra were recorded for a solid-state sample, due to intermolecular interactions and crystalline field effects in the sample, minor variations in the peak positions have been observed. This lowering of the stretching frequency from the computed values with a decrease in the intensity has been explained in terms of the electronic effects caused by back-donation[66] and induced by the oxygen atom.[66,67,70,74–76] The strong asymmetric bending vibration of the methyl in the methoxy groups appear at 1455, 1558 and 1470 cm^{-1} in the (B3LYP), (HF) and (Exp.) IR spectra, respectively. Whereas weak and very weak intensity components at 1472, 1475 and 1482 cm^{-1} in the (B3LYP), (HF) and (Exp.) Raman spectra, respectively.[77] The medium intensity band at 1470 cm^{-1} in the IR spectrum has been tentatively assigned to the asymmetric bending mode of the CH_3 group. The symmetric methyl deformation mode in the IR transmittance spectra was found at 1381 (B3LYP), 1346 (HF) and 1398 (Exp.) cm^{-1} and in the Raman spectra at 1357 (B3LYP), 1346 (HF) and 1394 (Exp.) cm^{-1}. The asymmetric and symmetric deformation modes shift to higher wavenumber by about 25–50 cm^{-1} when compared to the calculated results (Table S2†) and was attributed to electronic effects and strengthening of the bonding in the molecule. The CH_3 rocking vibrations are mixed with the C–O stretching and C–H bending modes, which results in a strong peak with a weak band component at 1144 and 1122 cm^{-1} in the IR (BL3YP) spectrum and as a medium intensity band with a weak component at 1144 and 1128 cm^{-1}, respectively.

4.2.2.2. Vibrations of the phenyl ring. In the 2,4,5-TMBC molecule, the two phenyl rings are bonded to the 1 and 3 position of prop-2-en-1-one as 4-bromophenyl (ring 1) and 2,4,5-trimethoxyphenyl (ring 2) groups. The benzene ring belongs to the D_{6h} symmetry group with effective symmetry of C_{2v} or lower due to all twenty vibrations being allowed in either IR or Raman spectroscopy. In these investigations, Herzberg's numbering system consistent with the logical scheme has been adopted when compared to the Wilson numbering system that was first reported and applicable for benzene only.[71,72] The 16 modes of the e_{2g} mode of the C–C asymmetric stretching vibration modes of the two phenyl rings are observed at 1603 (ring 1) and 1522 (ring 2) cm^{-1} (B3LYP); 1617 (ring 1) and 1532 (ring 2) cm^{-1} (HF); and 1610 (ring 1) and 1560 (ring 2) cm^{-1} (Exp.) in the IR transmission spectra and at 1617 (ring 1) and 1532 (ring 2) cm^{-1} (HF), and 1617 (ring 1) and 1560 (ring 2) cm^{-1} (Exp.). Whereas the C–C symmetric stretching vibration 13 modes of e_{1u} vibration at ~1450 cm^{-1} and 9 modes of b_{2u} vibration at ~1300 cm^{-1} for these two phenyl rings were observed at 1418 (ring 1) and 1306 (ring 2) cm^{-1} (B3LYP); 1403 (ring 1) and 1303 (ring 2) cm^{-1} (HF); and 1442 (ring 1) and 1295 (ring 2) cm^{-1} (Exp.) in the IR transmission spectra and at 1395 (ring 1) and 1280 (ring 2) cm^{-1} (B3LYP); 1403 (ring 1) and 1276 (ring 2) cm^{-1} (HF); and 1455 (ring 1) and 1278 (ring 2) cm^{-1} (Exp.) from the vibrations of these two modes. The large intensity difference between the two phenyl rings C–C stretching vibrational modes was attributed to the electronic effects induced by substituting the three methoxy

and bromo groups in the rings. The IR transmission spectra exhibit C–H ring stretching modes at 1585 (ring 1) (HF) and 1587 (ring 1) (Exp.) and at 1499 (ring 2) (B3LYP), 1485 (ring 2) (HF) and 1511 (ring 2) (Exp.) cm^{-1}, respectively, whereas the Raman C–H ring stretching modes of ring 1 were only observed at 1572 (B3LYP), 1582 (HF) and 1575 (Exp.) cm^{-1}; ring 2 does not show these modes. The calculated peak values are quite near to the experimental peak positions. The 9 modes of the b_{2u} vibration was observed as strong bands in the IR spectrum at 1327 cm^{-1} and in the Raman spectrum at 1329 cm^{-1}. The simultaneous IR and Raman activation of the phenyl ring modes of the 16 (e_{2g}), 13 (e_{1u}) and 9 (b_{2u}) vibrations provide evidence for the charge transfer interactions between the donor and the acceptor groups through the π-system. In tetra-substituted benzene, the C–C–H in-plane bending modes 3(a_{2g}), 17(e_{2g})a, 14(e_{1u})b and 14 (e_{1u})b are found in the 1300–1000 cm^{-1} region.[70] The higher and lower wavenumber values of the e vibrations are represented by a and b, respectively. The strong band in the IR spectrum at 1144 cm^{-1} corresponds to the ring mode 14 (e_{1u})b. Mode 17(e_{2g})a was observed as a weak band in the Raman spectrum at 1188 cm^{-1}. The increase in intensity of these modes in the Experimental spectra was attributed to the presence of the strong electron donor substituents (OCH_3 groups).[65,66,70] The C–C–H out-of-plane bending vibration was expected to occur in the region around 1000–675 cm^{-1}.[66,70] The 19(e_{2u})a C–C–H out-of-plane bending vibration was observed as a weak band at 856 cm^{-1} in the IR (Exp.) spectrum and the 19(e_{2u})b mode was observed at 830 cm^{-1} in the Raman (Exp.) spectrum. The presence of this peak confirms the *para*-substitution of the phenyl ring. The modes corresponding to 11(e_{1g}) a were observed as a medium intensity and weak band at 742 cm^{-1} and 746 cm^{-1} in the IR transmittance (Exp.) and Raman spectrum, respectively, which was also in agreement with the theoretical results. In all the aromatic compounds, the carbon–hydrogen stretching vibrations occur in the 3100–3000 cm^{-1} region. The C–H stretching vibrations in the benzene derivatives arise from two non-degenerate modes, 1(a_{1g}) at 3081 cm^{-1} IR (Exp.) and 3083 cm^{-1} Raman (Exp.); 5(b_{1u}) at 3133 cm^{-1} Raman (Exp.) and two degenerate vibrations of e_{2g} (3033 and 3021 cm^{-1}) in the Raman (Exp.) spectra, e_{1u} 3041 cm^{-1} (calc.), *i.e.*, the vibrations 1, 5, 15 and 12 modes, respectively. A weak band at 3041 cm^{-1} in the Raman spectrum corresponds to the C–H stretching mode 12a. The weak band observed in the IR (Exp.) spectrum at 3081 cm^{-1} corresponds to mode 1 (a_{1u} vibration). In benzene, the fundamental vibrations of a_{1g} (990 cm^{-1}) and b_{1u} (1006 cm^{-1}) are the ring breathing and trigonal bending of the 1 and 6 modes, respectively. The trigonal ring bending mode was obtained as a medium intensity band in the IR (Exp.) spectrum at 1029 cm^{-1}. The strong IR active ring breathing modes of the substituted phenyl rings are observed in the 795–950 cm^{-1} region and these peaks were tentatively assigned as listed in Table S2.†

4.2.2.3. Ethylene bridge vibrations. The vibrations pertaining to the ethylene bridge are very sensitive to the degree of charge transfer between the donor and the acceptor groups; thus, such stretching modes are important to explore.[77] In 2,4,5-TMBC, the C8═C9 stretching mode was observed as a strong band at 1587 cm^{-1} in the IR (Exp.) spectrum and as a strong band at 1575 cm^{-1} in the Raman (Exp.) spectrum. The corresponding calculated mode was at 1585 cm^{-1} in the IR (HF) spectrum and at 1572 (B3LYP) and 1582 (HF) cm^{-1} in the Raman spectra. The strong bands in the Raman spectrum and a weak band in the IR spectrum or *vice versa* have been attributed to presence or even absence of inversion symmetry. The intra-molecular charge transfer from the donor to acceptor group through the single-double bond conjugation may induce large variations in the molecular dipole moment and molecular polarizability, therefore causing the activity in both the IR and Raman spectra.[74] Thus, the simultaneous activation of the C8═C9 stretching modes in both the IR and Raman spectra confirms the charge transfer interaction between the C═O group and phenyl ring through the ethylene bridge. It can be observed from Fig. 3 that the calculated modes at 1585 and 1582 cm^{-1} have strong peaks in both the Raman and IR spectra.

4.2.2.4. Carbonyl group vibrations. The wavenumber of the C═O stretch due to carbonyl group mainly depends on the bond strength, which in turn depends upon inductive, conjugative and steric effects, and the lone pair of electrons on oxygen. The C═O stretching vibration is expected to occur in the 1740–1640 cm^{-1} region. In the present case, a very strong C═O experimental band was observed at 1735 cm^{-1} in the IR (Exp.) spectrum with the theoretical value at 1739 cm^{-1} in the IR (HF) spectrum and its conjugation with the C═C stretching mode was obtained at 1654 and 1652 cm^{-1} in the IR (Exp.) and Raman (Exp.) spectra, respectively. These values are in agreement with the reported values.[65,66,68,74] The in-plane and out-of-plane C═O deformations modes were assigned at 626 and 538 cm^{-1} in the IR (Exp.) spectrum and at 537 and 500 cm^{-1} in the Raman (Exp.) spectrum.

4.2.2.5. C–Br vibrations. C–Br stretching vibrations are observed below 700 cm^{-1}. For the 2,4,5-TMBC crystal, the C–Br asymmetric and symmetric stretching modes appear at 707 (B3LYP), 667, 646 (HF) and 647 (Exp.) cm^{-1} and at 448 (B3LYP), 417 (HF) and 437 (Exp.) cm^{-1}, respectively, in the IR spectra, whereas in Raman spectra these modes have been observed at 668 (B3LYP), 689 (HF), 703 (Exp.) cm^{-1} and at 445 (B3LYP), 453 (HF) and 437 (Exp.) cm^{-1}, respectively. These values are in agreement with the reported values.[66,67,69–72]

4.2.2.6. Understanding NLO activity by vibrational spectroscopy. The vibrational contribution to non-linear optical (NLO) activity has been characterized by the π-conjugated systems present in a molecule. Such systems have large value second order molecular polarizabilities, which encourage the activity of some modes in both the IR and Raman spectra. In this case, the simultaneous activity of the phenyl ring 16 and 9 modes in the IR and Raman spectra have been observed and play a crucial role in the NLO activity of the crystal. These modes split into 16a and 16b, and 9a and 9b peaks. The bands observed in the IR (Exp.) spectrum at 1587, 1442 and 1324 cm^{-1} are active in the Raman (Exp.) spectrum at 1575, 1455 and 1358 cm^{-1}, respectively. The relative intensities of both the IR and Raman peaks are comparable due to the electron cloud movement through the π-conjugated skeletal structure *i.e.* from the electron donor to electron acceptor group.

4.3. Electro-optical properties

4.3.1 Frontier molecular orbital (FMO) analysis. In the reactivity of any molecule, the frontier molecular orbitals (FMOs) play a vital role. Among the FMOs, the interaction of the HOMO and LUMO between the reacting species is very significant for the progress of a chemical reaction during compound formation through the stabilization of the transition state structure of any compound. The HOMO and LUMO energy values were determined at different levels of theory such as B3LYP, HF, CAM-B3LYP, wb97xd and LC-BLYP. The values calculated at the B3LYP level of theory are presented in Table 2. These energy gap values describe the chemical reactivity, kinetic stability, optical polarizability and chemical softness of any molecule. Molecules with a larger HOMO–LUMO energy gap are known as hard molecules and also possess higher thermal and kinetic stabilities according to softness-hardness rule. The energy gap between the HOMO and LUMO of 2,4,5-TMBC molecule was found to be 3.374 eV at the B3LYP/6-31G* level of theory with a chemical hardness value of 1.687 eV, which indicates that 2,4,5-TMBC has good kinetic stability.

TD-DFT calculations predict the electronic transition at 3.103 eV (see Table S3 of the ESI†) at the B3LYP level of theory corresponding to the transition from the ground state to the first excited state and shows charge transfer from the HOMO to LUMO. The 3D plots of the frontier molecular orbitals (FMOs) are shown in Fig. 4 and their respective energy values (in eV) are given in Table 4.

It can be observed from Fig. 4 that the HOMO are mainly delocalized on one side of the molecule, whereas the LUMO are delocalized almost over the whole molecule. The electronic density distribution is present on the whole molecule as indicated by HOMO–LUMO transition. In addition, this transition shows the intra-molecular charge transfer in the 2,4,5-TMBC molecule. The title molecule has advantages of noteworthy transparency and low absorbance as observed experimentally.[16,42] This was also confirmed by the theoretically calculated value of the transition energy, which was relatively larger and belongs to the violet region of the spectrum. The excitation energy calculated by the TDDFT method was found to be in good agreement with the HOMO–LUMO energy gap at the same levels of theory, *i.e.* B3LYP.

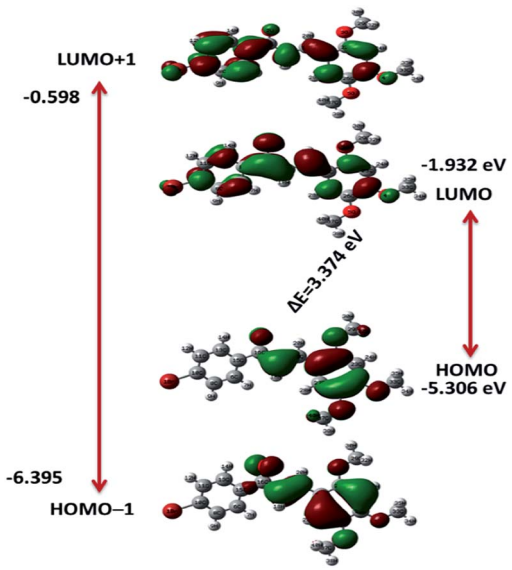

Fig. 4 The HOMO–*i* and LUMO+*i* (*i* = 0, 1) representation of 2,4,5-TMBC obtained at the B3LYP/6-31G* level of theory.

Table 4 The calculated energy values of the frontier molecular orbitals (FMOs) and energy difference of the HOMOs and LUMOs (in eV) at the B3LYP/6-31G* level of theory

Orbital	Energy
E_{HOMO}	−5.306
E_{HOMO-1}	−6.395
E_{LUMO}	−1.932
E_{LUMO+1}	−0.598
ΔE_{H-L}	3.374
$\Delta E_{H-1-L+1}$	5.796

4.3.2 Time dependent-density functional theory (TD-DFT) analysis. For excited state electronic structure calculations in quantum chemistry and solid state physics, time dependent density functional theory (TD-DFT) establishes itself as one of the most popular theoretical methods. Contemporary density functional approaches show a satisfactory balance between accuracy and computational efficiency when compared with traditional *ab initio* and semi-empirical approaches. We have applied a TD approach at the B3LYP, HF, range separated CAM-B3LYP, wb97xd and long range corrected LC-BLYP levels of theory with the 6-31G* basis set to examine the nature of the electronic transitions of 2,4,5-TMBC in the gas phase. As per the available literature, a precise absorption wavelength at moderately small computing time can be detected easily by such studies on the basis of the optimized ground state geometry, which corresponds to the vertical electronic transitions in the molecule.[78–80] The experimental UV-vis-NIR spectra of 2,4,5-TMBC has been previously reported in the literature.[16,42] The absorption wavelength, excitation energies, oscillator strengths and major contributions were calculated in the gas phase in the ground state of the optimized geometry and are presented in Table S3.† The calculated UV-vis spectra (obtained from the B3LYP, HF, CAM-B3LYP, wb97xd and LC-BLYP levels of theory) of 2,4,5-TMBC in the gas phase are shown in Fig. 5. As clearly observed from Fig. 5, there is a great difference in the values of the absorption wavelengths calculated using the different methods. We have compared our theoretically calculated absorption wavelength with the experimental value, *i.e.*, about 400 nm (the obtained spectra is shown in Fig. S3 of the ESI†)[42] and found that the value calculated at the TD-B3LYP/6-31G* levels of theory (400 nm) was in good agreement when compared with other applied methods (Table S3†). The optimized geometry of 2,4,5-TMBC specifies that the visible absorption maxima of this molecule corresponds to the electron transition from the HOMO to the LUMO.

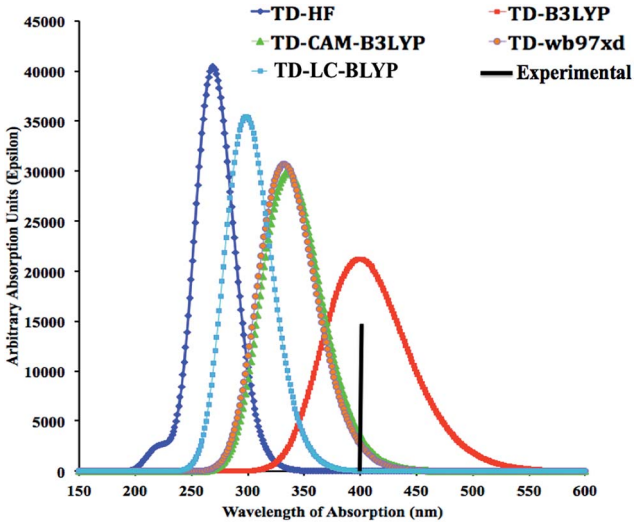

Fig. 5 UV-visible spectra of 2,4,5-TMBC calculated at different levels of theory using the 6-31G* basis set.

4.4. Polarizability and first hyperpolarizability

In non-linear optical processes of technological importance in device fabrications, the hyperpolarizability plays a significant role and vindicates the growing exertion ardent to the precise determination of this property.[81,82] Several recent studies[83–85] show that besides an appropriate treatment of electron correlation and a cautious choice of the function basis set, the inclusion of the contributions arising from nuclear motion is of fundamental importance for the calculations of molecular electrical properties such as polarizability and hyperpolarizability. Therefore, we have calculated the electronic total dipole moment (μ_{tot}), molecular total and anisotropy of polarizability (α_{tot}, $\Delta\alpha$), and static and total first hyperpolarizability (β_0, β_{tot}) using different methods such as the B3LYP, HF, range separated CAM-B3LYP, wb97xd and long range correction LC-BLYP levels of theory at the 6-31G* basis set. The calculated values at the B3LYP level of theory are presented in Table 5 along with 10 components. The values calculated at the HF, CAM-B3LYP, wb97xd and LC-BLYP levels of theory are also presented for comparison in Table S4(1–4) (see ESI data†). The polarizability and hyperpolarizability values are dominated by their diagonal components, *i.e.* components along the dipole moment axis of α_{xx} and β_{xxx}. The value of the total dipole moment (μ) was 2.343 D at the B3LYP level of theory. The variation of the hyperpolarizability values at all the applied levels of theory are shown in Fig. S4† along with those found for urea. From the figure it is clear that the hyperpolarizability value was found to be higher at the B3LYP level of theory than the other methods studied.

The highest value for μ_x of the dipole moment components was found and was a major contributor to the total dipole moment in the molecule. In a similar way, the average polarizability (α_{tot}), anisotropy of polarizability ($\Delta\alpha$) and total first hyperpolarizability (β_{tot}) of 2,4,5-TMBC have non-zero values of 46.699×10^{-24}, 39.626×10^{-24} and 21.137×10^{-30} esu, respectively. The non-zero value of β_{tot} shows that the title molecule possesses microscopic first static hyperpolarizability acquired by the algebraic second-derivative of the electric dipole moment. The first hyperpolarizability value of 2,4,5-TMBC is 56 times larger than that found for urea [the β value for urea is 0.3728×10^{-30} esu]. The experimental value for the second harmonic generation (SHG) of 2,4,5-TMBC was measured and found to be 1.8 times higher than that found for urea.[42] The calculated non-zero β_{tot} and SHG values were many folds higher than organic as well as other reported materials.[37–40,86–93]

4.5. Ionization potentials, electron affinities and reorganization energies

To shed light on the charge transport behavior, the ionization potential (IP), electron affinity (EA), λ (h), and λ (e) are significant factors. The smaller/higher IP/EA values means that materials would be efficient hole/electron transporters. The

Table 5 The calculated values of polarizability, hyperpolarizability and dipole moment along with their individual tensor components of 2,4,5-TMBC at the B3LYP/6-31G* level of theory[a]

Polarizability and dipole moment			Hyperpolarizability		
Components	a.u.	esu ($\times 10^{-24}$)	Component	a.u.	esu ($\times 10^{-30}$)
α_{xx}	460.421	29.34	β_{xxx}	−4463.056	−38.565
α_{xy}	−0.808	4.30	β_{xxy}	2214.039	19.132
α_{yy}	242.662	36.75	β_{xyy}	−193.007	−1.668
α_{xz}	−6.288	8.00	β_{yyy}	35.940	0.311
α_{yz}	7.913	−4.74	β_{xxz}	96.447	0.833
α_{zz}	99.245	32.90	β_{xyz}	−20.389	−0.176
α_{tot}	315.177	46.699	β_{yyz}	2.185	0.019
$\Delta\alpha$	267.443	39.626	β_{xzz}	39.080	0.338
μ_x	2.257	5.738 D	β_{yzz}	8.380	0.072
μ_y	−0.622	−1.582 D	β_{zzz}	−5.127	−0.044
μ_z	−0.078	−0.197 D	β_0	1467.657	12.682
μ_{tot}	2.343	5.955 D	β_{tot}	2446.095	21.137

[a] For α, 1 a.u. = 0.1482×10^{-24} esu, for β, 1 a.u. = 0.008629×10^{-30} esu, $\mu_{urea} = 1.3732$ D and $\beta_{urea} = 0.3728 \times 10^{-30}$ esu.[86]

smaller λ (h) and λ (e) values reveal proficient hole and electron transport materials, respectively. We have tabulated the IP_a, IP_v, EA_a, EA_v, λ (h) and λ (e) values in Table 6. The smaller IP_a/IP_v values of the chalcone derivative studied compared to 4,6-di(thiophen-2-yl)pyrimidine, *i.e.*, 0.99/0.88 eV show that 2,4,5-TMBC would be proficient hole transport material when compared to 4,6-di(thiophen-2-yl)pyrimidine.[57,94–96] The larger EA_a/EA_v values of the chalcone derivative compared to 4,6-di(thiophen-2-yl)pyrimidine, *i.e.*, 0.11/0.7 eV show that the former would be superior electron transporter when compared to the latter. The smaller computed λ (e) value of the chalcone derivative compared to the λ (h) value demonstrates that it would be a better electron transport material.

The major alteration from neutral geometry to cationic and anionic has been found in the C_{15}–C_{16}–C_{17} and C_{17}–C_{19}–C_{21} bond angles. The neutral, cationic and anionic bond angles in C_{15}–C_{16}–C_{17} (C_{17}–C_{19}–C_{21}) have been observed as 118.97°, 119.07° and 119.70° (127.90°, 127.17° and 126.88°), respectively. The key alteration in the geometry was observed from the neutral to cationic bond angles, *i.e.*, 0.73° and 1.02°. Thus, the geometry relaxation between the neutral and cationic are greater than the anionic bond angles ensuing more polarization in former and consequently, the λ (h) value is larger than the λ (e) value.

4.6. Global chemical reactivity descriptors (GCRD)

The parameters of the global chemical reactivity descriptors (GCRD) are very important to investigate the connection between the structure, stability and global chemical reactivity of molecules and are based on conceptual DFT. These descriptors are used in the expansion of quantitative structure–activity, structure–property and structure–toxicity relationships. The hardness of any molecule is related to its aromaticity.[97] DFT provides an explanation of the principal universal perceptions of molecular structure, stability and reactivity.[98] In the current study, we have calculated various GCRD using E_{HOMO} as the ionization potential (I) and E_{LUMO} as electron affinity (A) (details can be found in ESI†). The computed values of GCRD such as η, μ, S, χ and ω are 1.687, −3.619, 0.733, 3.619 and 1.809 eV, respectively at the B3LYP/6-31G* level of theory. Thermodynamic parameters, such as thermal energy (E), specific heat (C_v) and entropy (S) were calculated at the HF, B3LYP, CAM-B3LYP, wb97xd and LC-BLYP levels of theory with the 6-31G* basis set, and have been tabulated in Table S5 (ESI†). The variation of these thermodynamic parameters at the different levels of theory is shown in Fig. S5 (ESI†).

Table 6 The vertical and adiabatic ionization potentials (IP_v/IP_a), vertical and adiabatic electronic affinities (EA_v/EA_a) and hole/electron reorganization energies λ (h)/λ (e) of 2,4,5-TMBC studied at the B3LYP/6-31G* level of theory

Parameters	IP_v	IP_a	EA_v	EA_a	λ (h)	λ (e)
Units	eV	eV	eV	eV	eV	eV
Values	6.80	6.59	0.50	0.65	0.447	0.305

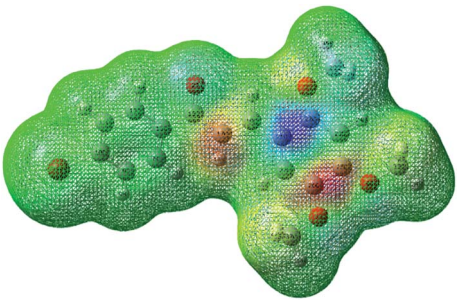

Fig. 6 The molecular electrostatic potential plot of 2,4,5-TMBC with an iso value of ±0.02 a.u.

4.7. Molecular electrostatic potential (MEP)

The 3D plot of the molecular electrostatic potential (MEP) of 2,4,5-TMBC was theoretically predicted to gain better understanding at a molecular level and is shown in Fig. 6. It is the measurement of the electrostatic potential on the constant electron density surface. The 3D plots of MEP overlap on the top of the total energy density surface. It is a very supportive property to investigate the reactivity of molecular species by predicting that either the approaching nucleophile is attracted towards a positive region of the molecule or the approaching electrophile is attracted towards a negatively charged surface of the molecule. In the MEP plot, the maximum positive potential (blue) and negative potential (red) regions are preferred sites for nucleophilic and electrophilic attack, respectively.[38,39,99,100] The MEP plot of 2,4,5-TMBC is drawn as shown in Fig. 6 to acquire simultaneous information on its molecular size, shape along with its positive, negative and neutral electrostatic potential regions in terms of color grading.

5. Conclusions

The ground state molecular geometry of 1-(4-bromophenyl)-3-(2,4,5-trimethoxyphenyl)prop-2-en-1-one was obtained using DFT and HF methods with the 6-31G* basis set. The calculated geometrical parameters at different levels of theory were compared to the experimental values and found to be in good agreement with one another. Furthermore, these geometrical parameters calculated by periodic boundary conditions at PBE/DNP were also found to be in good agreement with the experimental values reported. Spectral characterization has been carried out through FT-IR and FT-Raman analysis and found in respectable agreement with the experimental results. The lowering of the carbonyl stretching wavenumber indicates the presence of conjugation. The electronic effects of hyperconjugation and back-donation have also been established. The simultaneous IR and Raman activation of the phenyl ring modes of 16, 13 and 9 also provides evidence for the charge transfer interaction. Hydrogen bonding causes a downward wavenumber shift for the peaks. The intermolecular hydrogen bonds give broad bands, whereas intra-molecular hydrogen bonds produce sharp and well resolved peaks. The comprehensible intra-molecular charge transport has been observed

from the trimethoxyphenyl moiety (HOMO) to the bromophenyl unit (LUMO). The absorption wavelength determined at the TD-B3LYP/6-31G* level of theory in the gas phase was observed at ~400 nm, which was found to be in good agreement with the experimental value of 400 nm. The dipole moment and first hyperpolarizability values were found to be many folds (2 and 56 times calculated at the B3LYP level of theory) higher than that found for urea. The smaller geometry relaxation from neutral to anionic would lead to a smaller electron reorganization energy, which ultimately increases the electron charge transport. The smaller electron reorganization energy than the hole showed that 2,4,5-TMBC has great potential to be an efficient electron transport material. The calculated MEP plot shows the negative potential sites in the compound (as indicated by the red color), which is favorable for electrophilic attack, whereas the positive potential sites (as indicated by the blue color) are favorable for nucleophilic attack. The higher value of first hyperpolarizability makes it an excellent candidate for the fabrication of non-linear optical (NLO) devices.

Acknowledgements

The authors are thankful to King Khalid University, Abha, Saudi Arabia for providing the research infrastructure. One of the authors (P. S. Patil) is thankful to Science and Engineering Research Board (SERB), Government of India for providing Start-Up Research Grant under DST-SERB Scheme for Young Scientists (Grant No. SB/FTP/PS-021/2014).

References

1 M. Shigeru, M. Makoto, A. Hironaka and O. Susumu, *Biochem. Pharmacol.*, 1991, **42**, 1447–1451.
2 R. J. Anto, K. Sukumaran, G. Kuttan, M. Rao, V. Subbaraju and R. Kuttan, *Cancer Lett.*, 1995, **97**, 33–37.
3 S. Ducki, R. Forrest, J. A. Hadfield, A. Kendall, N. J. Lawrence, A. T. McGown and D. Rennison, *Bioorg. Med. Chem. Lett.*, 1998, **8**, 1051–1056.
4 F. Herencia, M. L. Ferrandiz, A. Ubeda, J. Domínguez, J. E. Charris, G. M. Lobo and M. J. Alcaraz, *Bioorg. Med. Chem. Lett.*, 1998, **8**, 1169–1174.
5 M. Liu, P. Wilairat and M.-L. Go, *J. Med. Chem.*, 2001, **44**, 4443–4452.
6 S. N. López, M. V. Castelli, S. A. Zacchino, J. N. Domínguez, G. Lobo, J. Charris-Charris, J. C. Cortés, J. C. Ribas, C. Devia and A. M. Rodríguez, *Bioorg. Med. Chem.*, 2001, **9**, 1999–2013.
7 J.-H. Wu, X.-H. Wang, Y.-H. Yi and K.-H. Lee, *Bioorg. Med. Chem. Lett.*, 2003, **13**, 1813–1815.
8 L. Mathiesen, K. E. Malterud and R. B. Sund, *Planta Med.*, 1995, **61**, 515–518.
9 B. Zhao, W.-Q. Lu, Z.-H. Zhou and Y. Wu, *J. Mater. Chem.*, 2000, **10**, 1513–1517.
10 X. Tao, T. Watanabe, K. Kono, T. Deguchi, M. Nakayama and S. Miyata, *Chem. Mater.*, 1996, **8**, 1326–1332.
11 V. Ramkumar, S. Anandhi, P. Kannan and R. Gopalakrishnan, *RSC Adv.*, 2015, **5**, 586–596.
12 V. Ramkumar, S. Anandhi, P. Kannan and R. Gopalakrishnan, *CrystEngComm*, 2013, **15**, 2438–2449.
13 M. Cockerham, C. Frazier, S. Guha and E. Chauchard, *Appl. Phys. B: Photophys. Laser Chem.*, 1991, **53**, 275–278.
14 P. S. Patil, V. M. Bhumannavar, M. S. Bannur, H. N. Kulkarni and G. Bhagavannarayana, *J. Cryst. Process Technol.*, 2013, **3**, 108–117.
15 R. Nithya, N. Santhanamoorthi, P. Kolandaivel and K. Senthilkumar, *J. Phys. Chem. A*, 2011, **115**, 6594–6602.
16 P. S. Patil, S. M. Dharmaprakash, K. Ramakrishna, H.-K. Fun, R. S. S. Kumar and D. N. Rao, *J. Cryst. Growth*, 2007, **303**, 520–524.
17 B. Gu, W. Ji, X.-Q. Huang, P. S. Patil and S. M. Dharmaprakash, *Opt. Express*, 2009, **17**, 1126–1135.
18 L. M. Saleh, H. A. Hassan, F. Z. Henari, P. S. Patil and M. S. Bannur, *Appl. Phys. B: Lasers Opt.*, 2014, **116**, 805–810.
19 J. Chen, X. Wang, Q. Ren, P. S. Patil, T. Li, H. Yang, J. Zhang, G. Li and L. Zhu, *Appl. Phys. B: Lasers Opt.*, 2011, **105**, 723–731.
20 B. Gu, W. Ji, P. S. Patil and S. M. Dharmaprakash, *J. Appl. Phys.*, 2008, **103**, 103511.
21 A. J. Kiran, H. Lee, H. Ravindra, S. Dharmaprakash, K. Kim, H. Lim and F. Rotermund, *Current Applied Physics*, 2010, **10**, 1290–1296.
22 T. Vijayakumar, I. H. Joe, C. R. Nair and V. Jayakumar, *Chem. Phys.*, 2008, **343**, 83–99.
23 D. Sajan, J. Binoy, I. Hubert Joe, V. Jayakumar and J. Zaleski, *J. Raman Spectrosc.*, 2005, **36**, 221–236.
24 J. Binoy, I. H. Joe and V. Jayakumar, *J. Raman Spectrosc.*, 2005, **36**, 1091–1100.
25 D. Sajan, I. H. Joe and V. Jayakumar, *J. Raman Spectrosc.*, 2006, **37**, 508–519.
26 S. Guidara, H. Feki and Y. Abid, *Spectrochim. Acta, Part A*, 2013, **115**, 437–444.
27 N. Elleuch, W. Amamou, A. B. Ahmed, Y. Abid and H. Feki, *Spectrochim. Acta, Part A*, 2014, **128**, 781–789.
28 B. G. Johnson, P. M. Gill and J. A. Pople, *J. Chem. Phys.*, 1993, **98**, 5612–5626.
29 S. Elleuch, H. Feki and Y. Abid, *Spectrochim. Acta, Part A*, 2007, **68**, 942–947.
30 M. Shkir and H. Abbas, *Spectrochim. Acta, Part A*, 2014, **125**, 453–457.
31 N. Sudharsana, S. Muthunatesan, G. J. Priya, V. Krishnakumar and R. Nagalakshmi, *Spectrochim. Acta, Part A*, 2014, **121**, 53–62.
32 A. Reshak and W. Khan, *J. Alloys Compd.*, 2014, **592**, 92–99.
33 S. Azhagiri, S. Jayakumar, S. Gunasekaran and S. Srinivasan, *Spectrochim. Acta, Part A*, 2014, **124**, 199–202.
34 M. Shkir and H. Abbas, *Spectrochim. Acta, Part A*, 2014, **118**, 172–176.
35 M. Shkir, S. Muhammad, S. AlFaify, A. Irfan and I. Yahia, *Spectrochim. Acta, Part A*, 2015, **137**, 432–441.
36 A. Kumar, V. Deval, P. Tandon, A. Gupta and E. D. D'silva, *Spectrochim. Acta, Part A*, 2014, **130**, 41–53.
37 M. Shkir, H. Abbas, S. Kumar, G. Bhagavannarayana and S. AlFaify, *J. Phys. Chem. Solids*, 2014, **75**, 959–965.

38 M. Shkir, S. AlFaify, H. Abbas and G. Bhagavannarayana, *Mater. Chem. Phys.*, 2015, **155**, 36–46.
39 M. Shkir, S. Muhammad and S. AlFaify, *Spectrochim. Acta, Part A*, 2015, **137**, 432–441.
40 H. Abbas, M. Shkir and S. AlFaify, *Arabian J. Chem.*, DOI: 10.1016/j.arabjc.2015.02.011.
41 P. S. Patil, M. M. Rosli, H.-K. Fun, I. A. Razak and S. M. Dharmaprakash, *Acta Crystallogr., Sect. E: Struct. Rep. Online*, 2006, **62**, o4644–o4645.
42 P. S. Patil, M. S. Bannur, D. B. Badigannavar and S. M. Dharmaprakash, *Opt. Laser Technol.*, 2014, **55**, 37–41.
43 C. Lee, W. Yang and R. G. Parr, *Phys. Rev. B: Condens. Matter Mater. Phys.*, 1988, **37**, 785–789.
44 A. D. Becke, *J. Chem. Phys.*, 1993, **98**, 5648–5652.
45 R. Dennington, T. Keith and J. Millam, *Semichem Inc.*, Shawnee Mission, KS, 2009.
46 T. Stein, L. Kronik and R. Baer, *J. Chem. Phys.*, 2009, **131**, 244119.
47 B. M. Wong and J. G. Cordaro, *J. Chem. Phys.*, 2008, **129**, 214703.
48 J. P. Perdew, K. Burke and M. Ernzerhof, *Phys. Rev. Lett.*, 1996, **77**, 3865–3868.
49 A. B. Nadykto, A. Al Natsheh, F. Yu, K. V. Mikkelsen and J. Herb, in *Adv. Quantum Chem.*, ed. E. G. Michael and S. J. Matthew, Academic Press, 2008, vol. 55, pp. 449–478.
50 B. Delley, *J. Chem. Phys.*, 2000, **113**, 7756–7764.
51 R. A. I., *Materials Studio Modeling*, San Diego, 2004.
52 S. Muhammad, A. Irfan, M. Shkir, A. R. Chaudhry, A. Kalam, S. AlFaify, A. G. Al-Sehemi, A. Al-Salami, I. Yahia and H. L. Xu, *J. Comput. Chem.*, 2015, **36**, 118–128.
53 S. Muhammad, H. Xu, M. R. S. A. Janjua, Z. Su and M. Nadeem, *Phys. Chem. Chem. Phys.*, 2010, **12**, 4791–4799.
54 D. Kleinman, *Phys. Rev.*, 1962, **126**, 1977.
55 M. J. Frisch, G. W. Trucks, H. B. Schlegel, G. E. Scuseria, M. A. Robb, J. R. Cheeseman, G. Scalmani, V. Barone, B. Mennucci, G. A. Petersson, H. Nakatsuji, M. Caricato, X. Li, H. P. Hratchian, A. F. Izmaylov, J. Bloino, G. Zheng, J. L. Sonnenberg, M. Hada, M. Ehara, K. Toyota, R. Fukuda, J. Hasegawa, M. Ishida, T. Nakajima, Y. Honda, O. Kitao, H. Nakai, T. Vreven, J. A. Montgomery Jr, J. E. Peralta, F. Ogliaro, M. Bearpark, J. J. Heyd, E. Brothers, K. N. Kudin, V. N. Staroverov, R. Kobayashi, J. Normand, K. Raghavachari, A. Rendell, J. C. Burant, S. S. Iyengar, J. Tomasi, M. Cossi, N. Rega, J. M. Millam, M. Klene, J. E. Knox, J. B. Cross, V. Bakken, C. Adamo, J. Jaramillo, R. Gomperts, R. E. Stratmann, O. Yazyev, A. J. Austin, R. Cammi, C. Pomelli, J. W. Ochterski, R. L. Martin, K. Morokuma, V. G. Zakrzewski, G. A. Voth, P. Salvador, J. J. Dannenberg, S. Dapprich, A. D. Daniels, O. Farkas, J. B. Foresman, J. V. Ortiz, J. Cioslowski and D. J. Fox, Gaussian, Inc., Wallingford CT, 2009, p. 9096580.
56 R. A. Marcus and N. Sutin, *Biochim. Biophys. Acta, Rev. Bioenerg.*, 1985, **811**, 265–322.
57 A. Irfan, *Comput. Mater. Sci.*, 2014, **81**, 488–492.
58 J. L. Brédas, J. P. Calbert, D. A. da Silva Filho and J. Cornil, *Proc. Natl. Acad. Sci. U. S. A.*, 2002, **99**, 5804–5809.
59 A. Irfan, A. G. Al-Sehemi, S. Muhammad, A. R. Chaudhry, A. Kalam, M. Shkir, A. E. Al-Salami and A. M. Asiri, *J. Saudi Chem. Soc.*, DOI: 10.1016/j.jscs.2014.12.009.
60 A. G. Al-Sehemi, A. Irfan and A. M. Asiri, *Chin. Chem. Lett.*, 2014, **25**, 609–612.
61 F. H. Allen, O. Kennard, D. G. Watson, L. Brammer, A. G. Orpen and R. Taylor, *J. Chem. Soc., Perkin Trans. 2*, 1987, S1–S19.
62 P. S. Patil, J.-J. Teh, H.-K. Fun, I. A. Razak and S. M. Dharmaprakash, *Acta Crystallogr., Sect. E: Struct. Rep. Online*, 2006, **62**, o3096–o3098.
63 P. S. Patil, J.-J. Teh, H.-K. Fun, I. A. Razak and S. M. Dharmaprakash, *Acta Crystallogr., Sect. E: Struct. Rep. Online*, 2006, **62**, o896–o898.
64 P. S. Patil, J. B.-J. Teh, H.-K. Fun, I. A. Razak and S. M. Dharmaprakash, *Acta Crystallogr., Sect. E: Struct. Rep. Online*, 2006, **62**, o1710–o1712.
65 N. B. Colthup, L. H. Daly and S. E. Wiberley, *Introduction to Infrared and Raman Spectroscopy*, Academic Press, New York, 1990.
66 G. Socrates, *Infrared characteristic group frequencies*, Wiley, Chichester, New York, 1980.
67 F. R. Dollish, W. G. Fateley and F. F. Bentley, *Characteristic Raman frequencies of organic compounds*, John Wiley & Sons, New York, 1997.
68 B. C. Smith, *Infrared spectral interpretation: a systematic approach*, CRC press, 1998.
69 N. P. Roeges, *A guide to the complete interpretation of infrared spectra of organic structures*, Wiley, 1994.
70 G. Varsanyi, *Vibrational Spectra of Benzene Derivatives*, Academic Press, New York, 1969.
71 G. Varsányi, *Assignments for vibrational spectra of seven hundred benzene derivatives*, Halsted Press, 1974.
72 F. A. Miller, *J. Raman Spectrosc.*, 1988, **19**, 219–221.
73 M. Gussoni and C. Castiglioni, *J. Mol. Struct.*, 2000, **521**, 1–18.
74 D. Sajan, J. Binoy, I. Hubert Joe, V. S. Jayakumar and J. Zaleski, *J. Raman Spectrosc.*, 2005, **36**, 221–236.
75 D. Sajan, I. H. Joe, J. Zaleski and V. S. Jayakumar, *Laser Phys. Lett.*, 2005, **2**, 343–350.
76 C. Castiglioni, M. Del Zoppo and G. Zerbi, *J. Raman Spectrosc.*, 1993, **24**, 485–494.
77 M. Tommasini, C. Castiglioni, M. Del Zoppo and G. Zerbi, *J. Mol. Struct.*, 1999, **480–481**, 179–188.
78 D. Jacquemin, J. Preat and E. A. Perpète, *Chem. Phys. Lett.*, 2005, **410**, 254–259.
79 D. Jacquemin, J. Preat, M. Charlot, V. Wathelet, J.-M. André and E. A. Perpète, *J. Chem. Phys.*, 2004, **121**, 1736–1743.
80 M. Cossi and V. Barone, *J. Chem. Phys.*, 2001, **115**, 4708–4717.
81 D. M. Bishop, *Adv. Quantum Chem.*, 1994, **25**, 1–45.
82 P. N. Prasad and D. J. Williams, *Introduction to nonlinear optical effects in molecules and polymers*, Wiley, New York, 1991.
83 V. E. Ingamells, M. G. Papadopoulos, N. C. Handy and A. Willetts, *J. Chem. Phys.*, 1998, **109**, 1845–1859.

84 S. Raptis, M. G. Papadopoulos and A. Sadlej, *J. Chem. Phys.*, 1999, **111**, 7904–7915.
85 U. Eckart, V. E. Ingamells, M. G. Papadopoulos and A. J. Sadlej, *J. Chem. Phys.*, 2001, **114**, 735–745.
86 K. Govindarasu and E. Kavitha, *Spectrochim. Acta, Part A*, 2014, **122**, 130–141.
87 C. Adant, M. Dupuis and J. Bredas, *Int. J. Quantum Chem.*, 1995, **56**, 497–507.
88 M. Karabacak and M. Cinar, *Spectrochim. Acta, Part A*, 2012, **86**, 590–599.
89 R. Raju, C. Y. Panicker, P. S. Nayak, B. Narayana, B. Sarojini, C. van Alsenoy and A. A. Al-Saadi, *Spectrochim. Acta, Part A*, 2015, **134**, 63–72.
90 R. N. Singh, A. Kumar, R. K. Tiwari, P. Rawat, V. Baboo and D. Verma, *Spectrochim. Acta, Part A*, 2012, **92**, 295–304.
91 K. Govindarasu and E. Kavitha, *Spectrochim. Acta, Part A*, 2014, **133**, 799–810.
92 K. Govindarasu, E. Kavitha and N. Sundaraganesan, *Spectrochim. Acta, Part A*, 2014, **133**, 417–431.
93 G. A. Babu and P. Ramasamy, *Mater. Chem. Phys.*, 2010, **119**, 533–538.
94 A. Irfan, A. G. Al-Sehemi and M. S. Al-Assiri, *J. Fluorine Chem.*, 2014, **157**, 52–57.
95 A. Irfan, A. G. Al-Sehemi and M. S. Al-Assiri, *Comput. Theor. Chem.*, 2014, **1031**, 76–82.
96 A. Irfan, *Optik*, 2014, **125**, 4825–4830.
97 A. Vektariene, G. Vektaris and J. Svoboda, *ARKIVOC*, 2009, **7**, 311–329.
98 R. G. Pearson, *J. Chem. Educ.*, 1987, **64**, 561.
99 J. S. Murray and K. Sen, *Molecular electrostatic potentials: concepts and applications*, Elsevier, 1996.
100 E. Scrocco and J. Tomasi, Electronic molecular structure, reactivity and intermolecular forces: An heuristic interpretation by means of electrostatic molecular potentials, in *Advances in Quantum Chemistry*, Academic Press, New York, 1978.

